

YOUR ARTICLE

Please review the proof* of your article carefully, checking for any final typographical errors or minor necessary updates. Please address and answer in full any queries which the copyeditor may have raised on the Author Query sheet accompanying your proofs.

Please make clear any necessary corrections, within **3 working days**, using one of the following methods:

- Use Adobe's Comments and/or Editing Tools to indicate changes directly onto the PDF and return via email. Please request guidelines if required.
- Email the necessary corrections as a list citing the page and line number where a correction needs to be made, how the text currently appears, and what it should be changed to.
- Use the British Standards Institution's proof marks to indicate changes on a paper printout of the PDF and email, fax or post the pages (contact details below).

Production Editor, MST, 1 Carlton House Terrace, London, SW1Y 5AF, UK, Tel.: 44 (0)20 7451 7359 Fax: 44 (0)20 7451 7307
mst@maneypublishing.com

VIEWING YOUR ARTICLE'S PRODUCTION STATUS AND PLACING ORDERS USING MANEYTRACK

<http://maneytrack.maney.co.uk>

Approximately two weeks ago, you will have received an email detailing your log-in details for Maney Publishing's web-based production tracking system, ManeyTrack. Via ManeyTrack you can:

- View the production status of your article at any time.
- Place orders for printed colour, offprints, issue copies, or to make your article open access.

Please log in using the web address, above. If you have misplaced your log-in details please check your spam/junk folder. If you are still unable to find them please click on the above url and click on 'Forgot Password' and follow instructions. If you require further technical assistance, please contact the Administrator: ManeyTrackAdmin@maneypublishing.com

ADDITIONAL INFORMATION

This journal is hosted online at www.maneyonline.com/mst

ADVANCE ARTICLES: Your article has been published online as an Advance Article, ahead of publication in an issue. It is now fully citable using its unique Digital Object Identifier (DOI). Any corrections which you make to your proof will be applied when the article is published in an issue. Corrections will be made prior to this only if the managing editor deems the error to be so serious as to affect the scientific validity.

Access to the full text of your Advance Article will only be available if your institution subscribes to the journal or if you have a personal subscription. However, once the article has been published in an issue you will receive by email a complimentary PDF eprint of the final version.

For further information about Advance Article publication please see www.maneyonline.com/page/authors/afteracceptance

OPEN ACCESS (MORE OpenChoice): Should you wish to make your article freely available online (open access) please log in to ManeyTrack to view prices and to place your order – see details for ManeyTrack above. For more information regarding Maney’s open access product, MORE OpenChoice, please see: www.maneyonline.com/openaccess

OFFPRINTS: You will receive a complimentary PDF eprint of your final article. If you wish to purchase traditional hardcopy offprints please log in to ManeyTrack to view prices and to place your order – see details for ManeyTrack above.

ISSUE COPIES: You will have the opportunity to purchase a copy or copies of the issue your article will be published in at the time you receive the final PDF (eprint) of your article. Details stating how to order will be included in the eprint email.

PRINTED COLOUR: All figures supplied as such will be reproduced online in colour free of charge. If you would like colour figures reproduced in the printed version please log in to ManeyTrack to view prices and to place your order – see details for ManeyTrack above.

GET FOUND, GET READ, GET CITED

As part of our commitment to making the content we publish as visible as possible, Maney offers its authors use of the Kudos service which is designed to help you increase article readership and citations by enabling you to explain, enrich and share your articles. Corresponding authors will receive a registration email regarding the service once the article is published. To find out more visit www.growkudos.com.

FEEDBACK

Tell us about your publishing experience at: https://www.surveymonkey.com/s/stm_authorsurvey

***Please note this PDF file may not be offered for commercial sale or for any systematic external distribution by a third party.**

Kind regards,
Production Editor

Multiscale 3D analysis of creep cavities in AISI type 316 stainless steel

T. L. Burnett^{*1,2}, R. Geurts², H. Jazaeri³, S. M. Northover³, S. A. McDonald^{1,4}, S. J. Haigh¹, P. J. Bouchard³ and P. J. Withers^{1,4}

A sample of AISI type 316 stainless steel from a power station steam header, showing reheat cracking, was removed from service and has been examined by a combination of microscale X-ray ~~computational tomography~~, nanoscale serial section ~~focused~~ ion beam–scanning electron microscopy, ~~elemental~~ energy dispersive X-ray ~~mapping~~ and transmission electron microscopy. Multiscale three-dimensional analysis using correlative tomography allowed key regions to be found and analysed with high resolution techniques. The grain boundary analysed was decorated with micrometre sized, faceted cavities, $M_{23}C_6$ carbides, ferrite and G phase but no σ phase. Smaller intragranular $M_{23}C_6$ particles were also observed, close to the grain boundaries. This intimate coexistence suggests that the secondary phases will control the nucleation and growth of the cavities. Current models of cavitation, based on isolated idealised grain boundary cavities, are oversimplified.

Keywords: Stainless steels, Creep cavitation, 3D imaging, Correlative tomography

14 This paper is part of a special issue on ...

Introduction

Nickel based alloys and heat resistant steels are generally the materials of choice for the construction of engineered components and plant operating at high temperatures. The creep lifetime of such materials is dependent on the applied load history, temperature and creep properties.¹ Various methods for estimating the remaining creep life of components have been developed including ductility exhaustion,² life fraction and phenomenological approaches incorporating cavitation or microstructural damage.³

Welding is widely used in fabricating systems for high temperature operation in the nuclear, aeroengine and oil and gas sectors. However, creep lifetimes can be reduced by the associated residual stresses.⁴ Furthermore, the transient thermal excursions arising from welding may produce suboptimal and inhomogeneous microstructures⁵ as well as interactions with the environment, for example, with carbon dioxide.⁶ Welds joining many heat resistant alloys, such as type 300 series stainless steels, alloy 800H, alloy 52 and alloy 617, are susceptible to reheat cracking. This creep failure mechanism is variously described in the literature as ductility dip cracking, relaxation cracking,

stress relief cracking, post-weld heat treatment cracking and strain age cracking.

In the 1990s, widespread reheat cracking was found in non-stress relieved welded AISI type 316H austenitic stainless steel components in several advanced gas cooled reactors (AGRs) in the UK.⁷ Interestingly, some of these were driven solely by the presence of residual stresses. Cracking in the heat affected zone (HAZ), a few millimetres from the weld fusion boundary, was caused by a combination of thermal relaxation of residual stress combined with very low material creep ductility (a fraction of 1%) at the operating temperature. The creep ductility of the HAZ of these welds was reduced owing to three effects: the thermomechanical plastic strains associated with welding, slow creep deformation rates such as those occurring under plant operational conditions⁸ and a highly triaxial residual stress state associated with the weld geometry.⁹ A ductility exhaustion life assessment model has been developed by the industry to predict the onset of reheat crack initiation in welded type 316H stainless steel components.^{2,8} Within this model, an empirical approach incorporating cavity nucleation and growth terms was adopted to describe the substantial effect of stress triaxiality on ductility.⁹ The model has been shown to overpredict damage for welded feature tests and laboratory specimens⁴ and continues to be applied to support operation of UK nuclear plants. However, the model lacks any direct functional relationship with the underlying damage development mechanisms. For example, it does not explain why reheat cracking appears to occur on a plane parallel to the fusion boundary, at initiation, rather than normal to the maximum principal macroscopic stress

¹School of Materials, University of Manchester, Manchester M13 9PL, UK

²FEI Company, Achtseweg Noord 5, Bldg 5651 GG, Eindhoven, The Netherlands

³Materials Engineering, The Open University, Walton Hall, Milton Keynes MK7 6AA, UK

⁴BP International Centre for Advanced Materials, School of Materials, University of Manchester, Manchester M13 9PL, UK

*Corresponding author, email timothy.burnett@manchester.ac.uk

direction (which acts along the welding direction and parallel to the crack plane), nor why the ductility of the HAZ can be an order of magnitude lower than the parent material.

The length scales of creep damage increase with time as the governing process changes from being diffusion driven, through cavity nucleation at grain boundaries and vacancy condensation around second phase particles, to cavity growth and linkage at the grain scale, followed ultimately by multigrain fissure and failure. For example, in AISI type 316 austenitic stainless steel, vacancy diffusion and dislocation mechanisms occur at subnanometre dimensions, and the minimum stable cavity diameter (i.e. nucleation size) is ~ 30 nm assuming a stress of 300 MPa (at 500°C) and a surface tension of 2.41 N m^{-1} for stainless steel.¹⁰ Evidence from reheat cracking studies using conventional optical microscopy suggests that such cavities often form around grain boundary carbides.¹¹ As cavities grow, they tend to coalesce to form microcracks having lengths of the order of the material's grain size (typically 50–100 μm), which then link up to form macrocracks a few millimetres long that can be detected and sized by non-destructive testing.

Methods used to observe and characterise creep damage in metals can be classified as either destructive or non-destructive and further subdivided into surface [two-dimensional (2D)] and volumetric [three-dimensional (3D)] methods. The capability of any technique is determined by its spatial resolution, the contrast mechanism, its sampling volume and by practical issues. Traditional procedures for direct optical microscopic examination of the surface of metallographic specimens can be applied to provide information about the location, size distribution and orientation of cavities and cracks greater than ~ 500 nm. At finer scales, scanning electron microscopy can, in theory, reveal details to a resolution of a few nanometres, but in practice, the size of cavities that can be observed is limited by the efficacy of traditional metallographic preparation techniques. At the highest resolutions, transmission electron microscopy (TEM) can be used to characterise very small cavities but the volume sampled is very small and specimens are difficult to prepare.

Small angle scattering (SANS) is a semidestructive technique, which can give population distributions of cavities and carbides in the size range of 10–500 nm^{11–13} and thereby provide indirect 3D observations typically in 20 mm³ sample volumes. However, observations have to be validated by other techniques to confirm the nature of the features being characterised.

New techniques for imaging the microstructure of material in three dimensions have emerged in recent years, most notably X-ray computational tomography (CT)¹⁴ and dual beam focused ion beam (FIB)–scanning electron microscopy (SEM) serial sectioning. For example, Pyzalla *et al.*,¹⁵ Gupta *et al.*,¹⁶ Sket *et al.*¹⁷ and Isaac *et al.*¹⁸ have applied X-ray CT to map creep cavitation damage at the micrometre scale. To cover a larger range of scales, region of interest (RoI) (also known as zoom or local tomography) can be performed.^{14,19} While conventional X-ray CT can map creep damage across relatively large volumes, it is insensitive to the grain boundaries and crystallographic relationships. Serial

section FIB tomography on the other hand samples volumes some 100 \times smaller but at a correspondingly higher spatial resolution (~ 10 nm).²⁰ Furthermore, it facilitates identification of the grain boundaries via electron backscattered diffraction as well as chemical mapping in 3D by energy dispersive X-ray (EDX). By incorporating both within a correlative tomography framework,²¹ we can survey damage at the larger scale and then select RoIs for higher resolution study by FIB tomography, ensuring that the information thus obtained is statistically and spatially relevant in terms of the macrostructure of the creep damage (e.g. the final creep crack).

In the present paper, we focus on a particular joint from a pressure vessel (a boiler steam header) removed from an operational AGR plant owing to the development of extensive reheat cracking.⁷ This component and cracking mode have been the focus of previous detailed examination by conventional optical microscopy, small angle neutron scattering^{11–13} and synchrotron tomography.²² Using FIB serial sectioning of RoIs located by X-ray microtomography, we explore in detail the local environment of the creep cavities, in an effort to understand how this may have affected their nucleation, growth and eventual coalescence, which led to macroscopic reheat cracking. Previous work¹² has suggested that there are significant variations in carbide and cavity populations local to the reheat crack (see Fig. 1), and in the present study, we look at cavitation at just one RoI. Ultimately, we hope to expand our study to look at the whole region because it is our aim to understand the coevolution of the secondary phases and cavitation damage and develop functional relationships between the nature of internal damage and macroscopic quantities such as stress, strain, temperature and time in order to improve methods of creep life prediction.

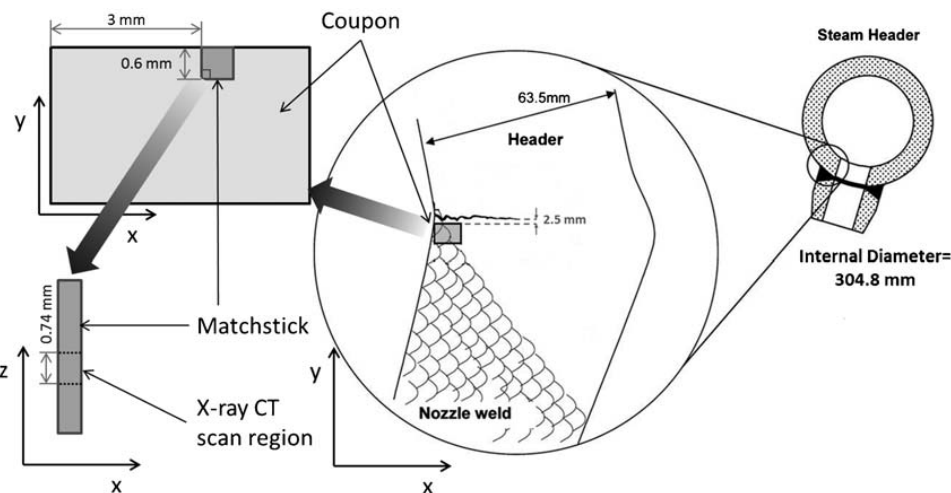
Experimental

Material composition and history

An AGR power station steam header (1C1/1 cast 55919) operating under internal pressure loading of 16 MPa at $\sim 525^\circ\text{C}$ was removed from service, after 65 000 h, following the detection of extensive creep cracking by non-destructive surface and ultrasonic volumetric inspections. A cross-sectional slice of material containing the cracked region was excised from the header to nozzle weld region, as indicated in Fig. 1. The header was made from AISI type 316H austenitic stainless steel with the composition shown in Table 1 and had a grain size of $85 \pm 10 \mu\text{m}$. A $\sim 10 \text{ mm}^2$ and ~ 8 mm thick coupon was extracted from a location before the crack mouth and the outer surface of the header for the present studies. The coupons were cut into a series of nominally 0.5 mm² cross-section matchsticks using a fine SiC circular saw. Multiple matchsticks were cut from each coupon, and their position within the coupon was recorded. The HAZ material associated with the nozzle attachment weld in this coupon has been previously identified as a region prone to high creep cavitation according to both numerical modelling and SANS experiments¹² (referred to as region number 12 in their work).

Correlative tomography strategy

The experimental method employed here has been termed 'correlative tomography'.²¹ It describes a multi-scale 3D method of characterisation where the same RoI

Online
colour
only

1 Schematic diagram showing where sample was extracted from ex-service steam header. Coupon was originally extracted close to crack origin from which smaller matchstick was extracted, which is subject of studies here. Coordinate system shows relative orientation of matchstick with respect to original component and crack. Schematic of matchstick sample shows region of X-ray CT analysis, 3D visualisation of which is shown in Fig. 2a

is interrogated at different scales and using different imaging modalities. Here, X-ray CT data are used to survey a large volume, in this case, a millimetre sized matchstick of material, but there is the potential to image the whole region local to the reheat crack at a lower magnification first before continuing to progressively higher resolution analyses. The role of the large volume X-ray CT scan on the matchstick was threefold: to provide an overview of the sample and the features of interest visible at this scale, to provide an intermediate scale linking the higher resolution analysis to the component scale and to provide a means for identifying and locating RoIs for higher resolution investigation in 3D using FIB-SEM serial sectioning. Once an RoI was identified (in this case, two RoIs were identified) by non-destructive X-ray CT (Fig. 2a and b) for higher resolution examination, features on the sample surface that were visible in the X-ray CT data were located in the FIB-SEM and used as a means of spatially correlating the two datasets (for further details, see Burnett *et al.*).²¹ Once correlated, it was possible to import knowledge about the location of the subsurface

RoI from the X-ray CT data into the coordinate system of the FIB-SEM. With the location of the RoIs defined in the FIB-SEM, the RoIs could be progressively revealed by serial sectioning using the FIB (Fig. 2c). In this manner, the same RoI can be imaged by X-ray CT and SEM, providing higher resolution insights and enabling crystallographic and potentially chemical information to be added to the picture. Once serial sectioning was complete, a thin slice of material was removed for analysis in the scanning transmission electron microscope (STEM) at an even higher resolution analysis (Fig. 2d) and crucially providing information on the chemistry and crystallography of the RoIs.

Microscale X-ray computed tomography

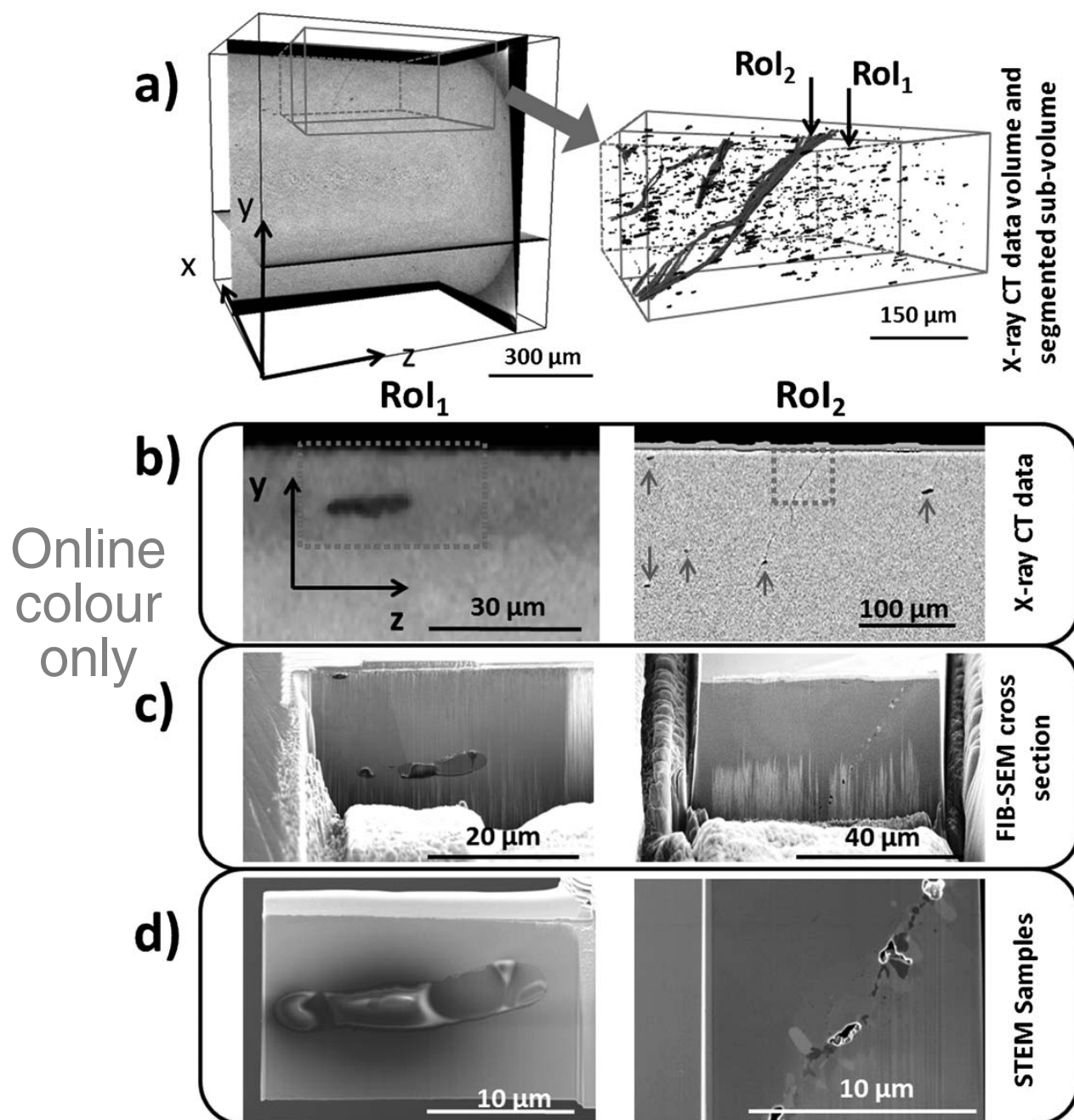
X-ray CT was carried out on the 'TOMCAT' synchrotron beamline at the Swiss Light Source in order to characterise the defect structure within a matchstick sample (of cross-section $\sim 0.6 \times 0.6$ mm) cut from a coupon located close to the reheat crack from the side nearest the crack (see Fig. 1). Projections (1501) over 360° were collected with energy of 38 keV and a 2 s exposure time per frame. The source detector distance was ~ 25 m, and the sample detector distance was as small as possible (5 mm). The 3D volume was reconstructed, using a Feldkamp–Davis–Kress reconstruction at a $0.37 \mu\text{m}^3$ voxel size (the smallest achievable for this set-up), before visualisation in 3D using Avizo software (see Fig. 2a). This 3D map was used to visualise the defects throughout the sample at the micrometre scale before more detailed analysis by electron microscopy.

Nanoscale serial section tomography

Two RoIs near the surface were identified from the X-ray CT dataset for further investigation: one containing prolate spheroidal feature that was ultimately identified as a stringer and one containing a 'dark line' feature (see Fig. 2a and b). After spatial correlation of the X-ray CT data to the sample surface imaged with an FEI Helios 650 Dualbeam FIB-SEM, the locations of the RoIs could be identified and a physical cross-section of each RoI was prepared using the Ga ion FIB. The cross-sections were then imaged using the electron beam

Table 1 Composition of AISI type 316H austenitic stainless steel header (while there is no direct confirmation of Nb content for this header, other headers from same cast have had their Nb content measured as 0.06 wt-%)

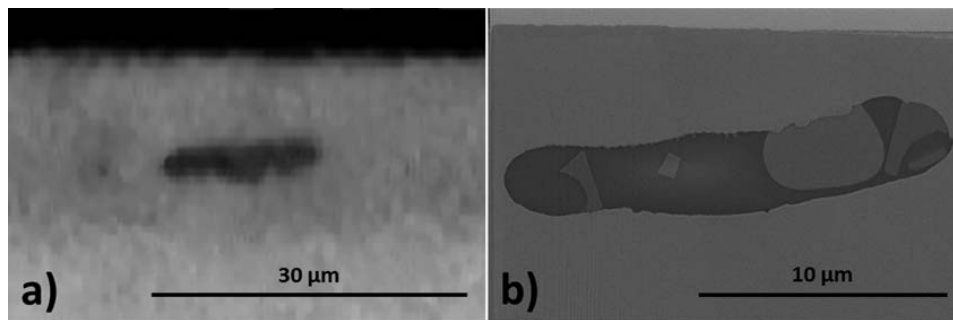
Composition/wt-%	Header	Weld
C	0.058	0.035
Si	0.42	0.46
Mn	1.61	0.94
P	0.009	0.011
S	0.020	0.010
Cr	17.33	18.36
Ni	11.29	11.36
Mo	2.31	2.91
Cu	0.12	0.04
V	0.04	0.06
Ti	<0.01	0.02
Al	<0.01	0.01
Co	<0.07	0.03
N	0.041	0.056



2 *a* left shows three unprocessed orthogonal virtual slices from reconstructed X-ray CT dataset. Total size of this volume was $0.74 \times 0.6 \times 0.6$ mm. Subvolume is indicated, which has been segmented for 3D visualisation of visible features. Two principal features are that of 'stringers' and 'dark lines'. Width of dark lines has been exaggerated in segmented volume to make them clearly visible at this scale. Approximate location of two Rols chosen for further analysis is indicated. *b* Rol₁ shows large stringer, which was chosen for further analysis (image processed with edge preserving smoothing and non-local means filters). Rol₂ shows dark line, which was chosen for further analysis; other stringers are visible in this virtual slice and indicated by blue arrows (image processed with adaptive histogram equalisation and median filter). For both images, region for FIB-SEM analysis is indicated by dashed red outline. *c* image (SEM) (using mixed signal of secondary and backscatter electrons via through lens detector) of FIB prepared cross-section of two same Rols imaged via X-ray CT in *b*. Already for Rol₁, feature can be identified as solid multiphase feature sitting on grain boundary and Rol₂ can be identified as a string of cavities. *d* image (SEM) showing detail of two same Rols once TEM lamella of the feature had been extracted. Rol₁ can now be clearly seen solid multiphase feature with some parts of structure charging under electron beam. Rol₂ shows detailed morphology some individual cavities that lie along boundary as well as wealth of secondary phases, which also exist there

and the through lens detector, collecting a mixture of secondary and backscatter electrons. A degree of caution was applied to the positioning of the first cross-section excised so as to just fall short of the feature

of interest. From this point, material was successively removed from the cross-section to uncover the features of interest. Any mislocation of the feature either laterally or with depth could be addressed at this stage to position



3 a post-processed (edge preserving smoothing and non-local means filtering) virtual slice from reconstructed X-ray CT data showing stringer in RoI₁ and b SEM image of same stringer in RoI₁ taken with through lens detector on extracted TEM lamella

the feature of interest in the centre of the cross-section where possible (see Fig. 2c). Once this initial cross-section had been prepared, this became the starting point for destructive serial sectioning of the feature using the Auto Slice and View software, whereby a sequence of cross-sections is prepared one after another using the FIB with each cross-section imaged by the SEM,²³ creating a high resolution 3D image volume (Fig. 4). A nominal slice thickness of 20 nm and a pixel size of $x=8.8$ nm and $y=11.2$ nm was used for the present work.

After the serial sectioning, but before completely slicing the entire feature, a thin (<5 µm) lamella of material from the same region was extracted for analysis in the STEM (see Fig. 2d). Once extracted, further thinning, using the FIB, was required to produce an electron transparent lamella for STEM imaging.

We have been careful to assess the damage introduced by the FIB-SEM serial sectioning. The fact that each slice in the series smoothly blends to the next in the series shows that not only have we chosen an appropriate slice thickness (~ 20 nm) but that there is no significant damage (see videos S1 and S2 in the supplementary information) or misalignment between slices. The faceted nature of the cavities is further evidence that the original morphology of these features is preserved. It is clear that limited damage by the way of curtaining is present (see Fig. 4a) and is particularly hard to avoid when sectioning materials that offer vastly different resistance to the ion beam (i.e. between the cavities and the steel matrix); however, the continuity of the features through the slice series has not significantly affected the shapes of the cavities.

Scanning transmission electron microscopy

As mentioned above, a thin (<5 µm) lamella of material from each RoI was extracted for analysis in the STEM after FIB-SEM serial sectioning. Once extracted and mounted onto a copper TEM grid, further thinning, using the FIB, was required to produce an electron transparent lamella for STEM imaging. Scanning transmission electron microscopy imaging and EDX spectrum imaging were performed using a probe side aberration corrected FEI Titan G2 80-200 S/TEM operated at 200 kV (Fig. 5). Images (STEM) were collected using a convergence angle of 18 mrad and a high angle annular dark field (HAADF) detector with an inner angle of 54 mrad. EDX spectroscopy and compositional analysis were performed using the Super-X detector configuration (4×30 mm silicon drift

detectors) with a solid angle of ~ 0.7 sr and a beam current of ~ 0.6 nA. Spectrum images were acquired with a dwell time of 30 µs per pixel. For display purposes, all elemental maps were processed using a three-pixel smoothing window in the Bruker Esprit software.

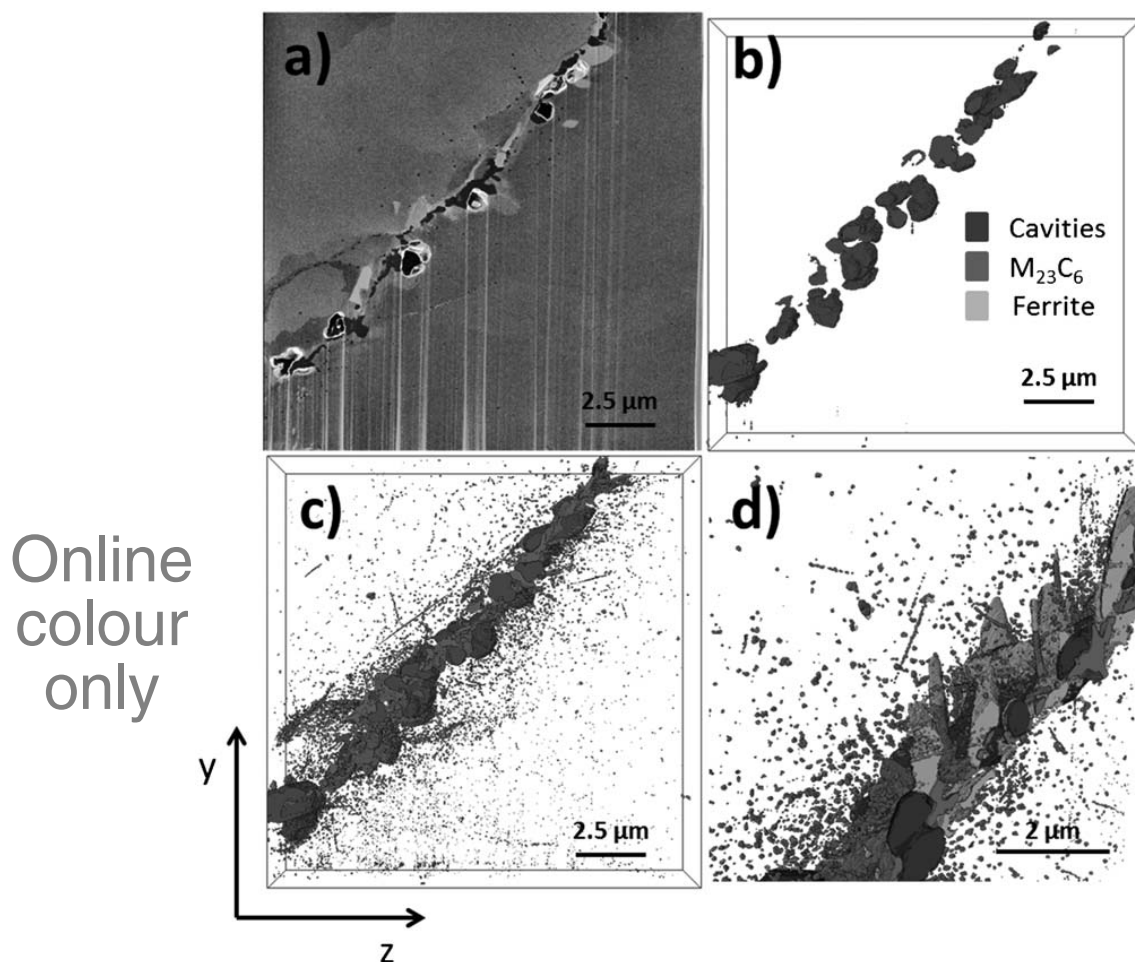
Energy dispersive X-ray spectrum images were also recorded in the FEI Helios 650 FIB-SEM as the sample extracted using the FIB was thicker than optimal for STEM analysis. All SEM-EDX spectroscopy measurements were made at 20 kV and high current using an Oxford Instruments Xmax80 EDX detector and Aztec software (see Fig. 6).

In all cases, the quantification of the EDX spectroscopy data extended only to the identification of the major, minor and trace elements.

Results

Overview

Figure 1 shows the orientation of the matchstick with respect to the original welded component. As can be seen in Fig. 2, there are two types of feature visible (what we have termed stringers and dark lines), which have then been segmented in the subvolume (Fig. 2a). Both of these features appear dark with respect to the steel matrix and lighter with respect to the air background in the virtual slices of the reconstructed dataset, indicating an electron density (i.e. function of density and/or atomic number) somewhere intermediate to the steel and the air (Fig. 2b). These stringers have a range of sizes, from ~ 20 µm down to the resolution limit of the X-ray CT imaging (~ 1 µm). It is evident from the X-ray CT data that these features are generally aligned along the length of the matchstick (i.e. along the axis of the header). ~~We have termed these cigar shaped (prolate spheroids) features 'stringers'.~~ Their appearance, as shown in Fig. 2a, is typical of what is observed in all locations so far surveyed across the header. Figure 2 shows the success of the 'correlative tomography' approach as we have been able to locate and section one of the stringers (RoI₁ in Fig. 2) identified from the X-ray CT data ready for higher resolution analysis using SEM and TEM. It should be noted that the total volume of the stringers in the volume measured is $<0.1\%$, highlighting the need for guidance in finding these features, which look densely populated in 3D are in fact quite disperse. Figure 3 confirms the stringer as a solid multiphase feature and provides a comparison of the feature as observed by X-ray and SEM. As can be seen,



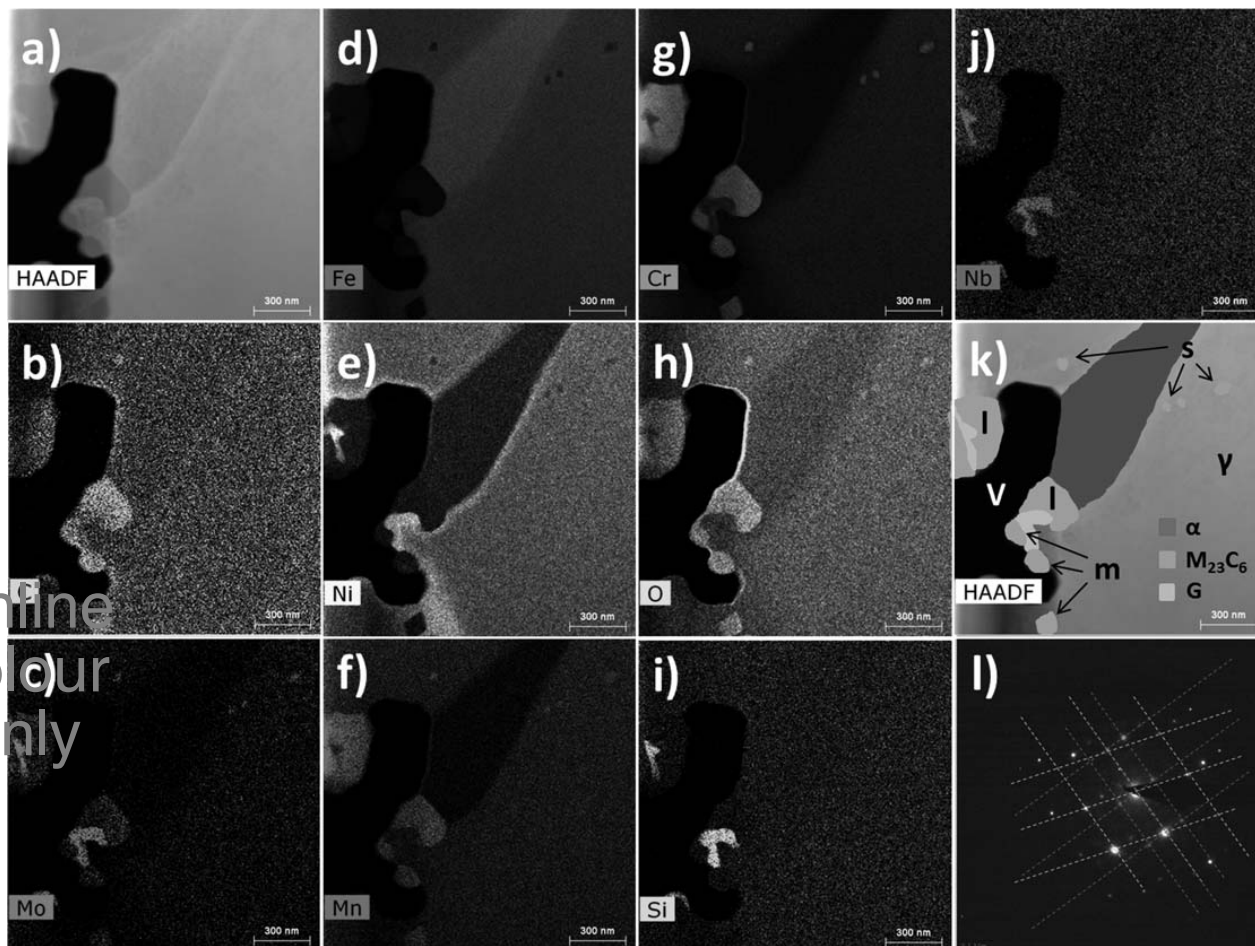
4 *a* unprocessed SEM image (using mixed signal of secondary and backscatter electrons via through lens detector) of representative region of cross-section created by FIB, one of series of images acquired during serial sectioning using Auto Slice and View. *b* 3D visualisation of cavities created after segmentation of FIB-SEM serial section volume. *c* 3D visualisation of cavities and $M_{23}C_6$ phase prepared in same way as *b*. *d* 3D visualisation of cavities, $M_{23}C_6$ and ferrite prepared in same way as *c* viewed from different perspective to show clearly the morphology of ferrite phase. Cavities are represented in blue, $M_{23}C_6$ phase in red and the ferrite in green as indicated by key in *b*

3

the shape orientation compares very favourably between the two. Multiple measurements from each image give an average length and height of the stringer of 17.5 and 4.1 μm (for the maximum height) as measured by X-ray CT and 18.662 and 3.650 μm as measured from the SEM image. This gives an agreement within 7% of the length and within 12% of the height which looks reasonable. While we have chosen comparative slices, we have not serially sectioned the entire feature so a degree of uncertainty remains in the position of the slice we have compared, so caution needs to be applied, and further measurements made, before, for example, altering the segmentation routine of the X-ray CT data.

Figure 2 shows again the success of the correlative tomography approach, this time in locating and sectioning in the FIB-SEM an example of what we have termed 'dark lines' from the virtual slices of the reconstructed X-ray CT data (RoI₂). These fine features are very difficult to segment in the X-ray CT data; they are shown in the visualisation of the subvolume in Fig. 2*a* (their width has been slightly exaggerated for easy viewing). As can be seen in the segmented subvolume of the X-ray CT data in Fig. 2, these features are always aligned at $\sim 45^\circ$ to the length of the matchstick. Looking at the XY plane presented in

Fig. 1, this would result in a 45° plane coming out of the surface in such a way that a slice through it, following the XY plane, would reveal a line parallel to the X direction, i.e. as would be observed from a physical cross-section or metallographically prepared sample. This orientation was consistently observed for a total of 8–10 'dark lines' found in this sample, although there is some uncertainty as to whether some of the dark lines are separate or connected. The physical cross-sections prepared using the FIB allowed identification of the 'dark lines' as boundaries decorated with cavities and multiple additional phases (see RoI₂ in Fig. 2*d*). The orientation of this boundary can be seen in the X-ray CT data in Fig. 2 from the YZ perspective. The contrast observed in these virtual slices is likely to be due to the presence of the cavities on the grain boundary with some influence from the other phases; this non-optimum contrast made it impossible to distinguish individual cavities from the X-ray CT alone. SAED in the TEM and STEM EDX spectrum imaging of a lamella prepared from this same region confirmed the 'dark line' as a grain boundary hosting a total of three phases identified in addition to the cavities (Fig. 5). The phases were $M_{23}C_6$, ferrite and G phase (Fig. 5*k*). High resolution 3D volumes obtained by serial sectioning



5 a Image (HAADF-STEM) from grain boundary showing faceted cavity in contact with different second phase particles and matrix. b–j elemental maps recorded using STEM EDX spectrum imaging of area shown in a. k schematic diagram overlaid onto HAADF image showing key to different phases identified by composition and selected area electron diffraction (SAED), V is cavity, α is ferrite, γ is austenite matrix and 's', 'm' and 'l' indicated small, medium and large $M_{23}C_6$ phase particles respectively. l SAED pattern from area labelled α in k; yellow grid is $[5-23]_{bcc}$ pattern and red grid is $[2-11]_{bcc}$ pattern

with the FIB containing the 'dark line' feature show the 3D arrangement of cavities and carbides around the grain boundary (see Fig. 4). This demonstrates very clearly the intimate association of the cavities with the second phases in the boundary.

$M_{23}C_6$

Our study has highlighted three distinct morphologies of the $M_{23}C_6$ carbides, namely, large irregular grain boundary particles that grow into the grains on both sides of the boundary, intermediate particles that also sit on the grain boundary but appear only grow into one grain, and small intragranular carbides (see Figs. 4c and d and 5k). Despite the three distinct morphologies, all appear to have the same composition (see Fig. 5). They are composed predominantly of Cr and C, as expected, but also contain Mo and Mn. As demonstrated in Fig. 5d, very little, if any, Fe is present in this phase, but its presence cannot be discounted completely. The large (500–2000 nm) $M_{23}C_6$ irregular carbides on the grain boundary have their maximum dimension typically along the grain boundary essentially forming discontinuous plates (see regions marked 'l' in Fig. 5k). The intermediate (100–300 nm) $M_{23}C_6$ carbide (see regions marked 'm' in Fig. 5k) particles also sit on the grain boundaries. Finally, there is a huge population of small

intragranular carbides (45–90 nm) (see regions marked 's' in Fig. 5k, and in red in Fig. 4c and d). Close inspection in the TEM reveals that these intragranular carbides are cuboidal in nature, although their small size means that they often appear spheroidal when viewed by SEM.

$M_{23}C_6$ is generally the first precipitate to form on aging 316 steels.^{24–27} At 525°C, $M_{23}C_6$ starts to form at grain boundaries after only a few tens of hours,²⁵ much earlier than is indicated on time–temperature–transformation curves generated by X-ray methods, which can detect precipitates only when present at overall levels >0.3 wt-%.²⁶ The transformation rate to $M_{23}C_6$ increases significantly with the concentrations of both C and Mo. Weiss and Stickler suggested that initially the $M_{23}C_6$ is a predominantly Cr/Fe carbide but that, over time, the molybdenum content increases to a composition of $(Fe, Cr)_{21}Mo_3C_6$. They also identified the presence of Mo in the $M_{23}C_6$. Mn is also seen to be present in the $M_{23}C_6$ here, consistent with the finding of Lai²⁴ that the solubility of Mn in $M_{23}C_6$ is 8%. Nucleation of $M_{23}C_6$ will occur first at high energy sites on grain boundaries or phase interfaces. Within the HAZ, nucleation will be most favoured on any ferrite–austenite boundaries because the δ ferrite is Cr and Mo rich and the austenite is C rich.²⁸ Austenite–austenite

grain boundaries are the next preferred nucleation site because grain edges and corners offer energetically favourable nucleation sites and diffusion is quickest along the grain boundaries. The precipitation of intragranular carbides also occurs, albeit more slowly, on twins, low angle boundaries and dislocations. Hence, the focus of these carbides on and around the grain boundary is seen in Fig. 4c and d and also shown by Jazaeri *et al.*¹¹ and Minami *et al.*²⁹ Previous SANS results³⁰ have detected a distribution of particles ~30 nm in size. Only a few particles close to this size, likely to be carbides, have been detected in the current study, but imaging was not optimised to observe such particles.

G phase

~~Scanning transmission electron microscopy~~, EDX spectrum imaging revealed small regions of what we have identified as G phase (*see* Fig. 5), which is a Ni, Nb and Si rich phase with small amounts of Fe and Cr²⁷ previously reported with a composition of 51Ni–29Nb–14Si–4.5Fe–1.5Cr (wt-%).³¹ The G phase also contains a surprisingly high level of Mo, which has not previously been reported as a constituent of this phase. The small size (smallest dimension typically <100 nm) of these particles has made examination using diffraction difficult. This appears to be the first time Nb rich G phase has been reported in an 18Cr–12Ni steel,²⁷ but both the diminutive size and the close proximity to multiple other phases would have made it quite easy to overlook in previous work. These particles were identified exclusively along the grain boundary and were intimately related to the $M_{23}C_6$ carbides.

Although the Nb content of this header is unknown, others from the same cast have had their Nb content measured as 0.06 wt-%. This would explain the presence of G phase, which has previously been observed to form in preference to σ phase at grain boundaries in Nb stabilised austenitic stainless steels. Aging (8000 h) of such material at 500°C produced G phase and $M_{23}C_6$ associated with each other at the grain boundaries,³¹ as found in the present study.

Ferrite

We have identified the presence of ferrite via STEM EDX and SAED in the TEM (*see* Fig. 5). Figure 4d shows that there are significant amounts of this ferrite growing away from the grain boundaries and the carbides, while none was found within the grains (rendered transparent here). The morphology of the ferrite is very striking; it is strongly faceted and grows away from the grain boundary (or more specifically it appears to initiate from the $M_{23}C_6$) into the matrix with a roughly triangular cross-section. The maximum observed length of the ferrite was ~2 μm . This 3D visualisation also reveals the abundance of ferrite in the region of the boundary. The ferrite's composition is Fe rich, and it appears to contain significantly lower concentrations of all the same constituents as the matrix. However, the detection of these elements will be influenced by the surrounding matrix, and it is therefore very difficult to completely exclude their presence in the ferrite phase. Of particular note is the segregation of nickel into the austenite matrix immediately around the ferrite (*see* the edge of the ferrite phase in Fig. 5e).

Cavities

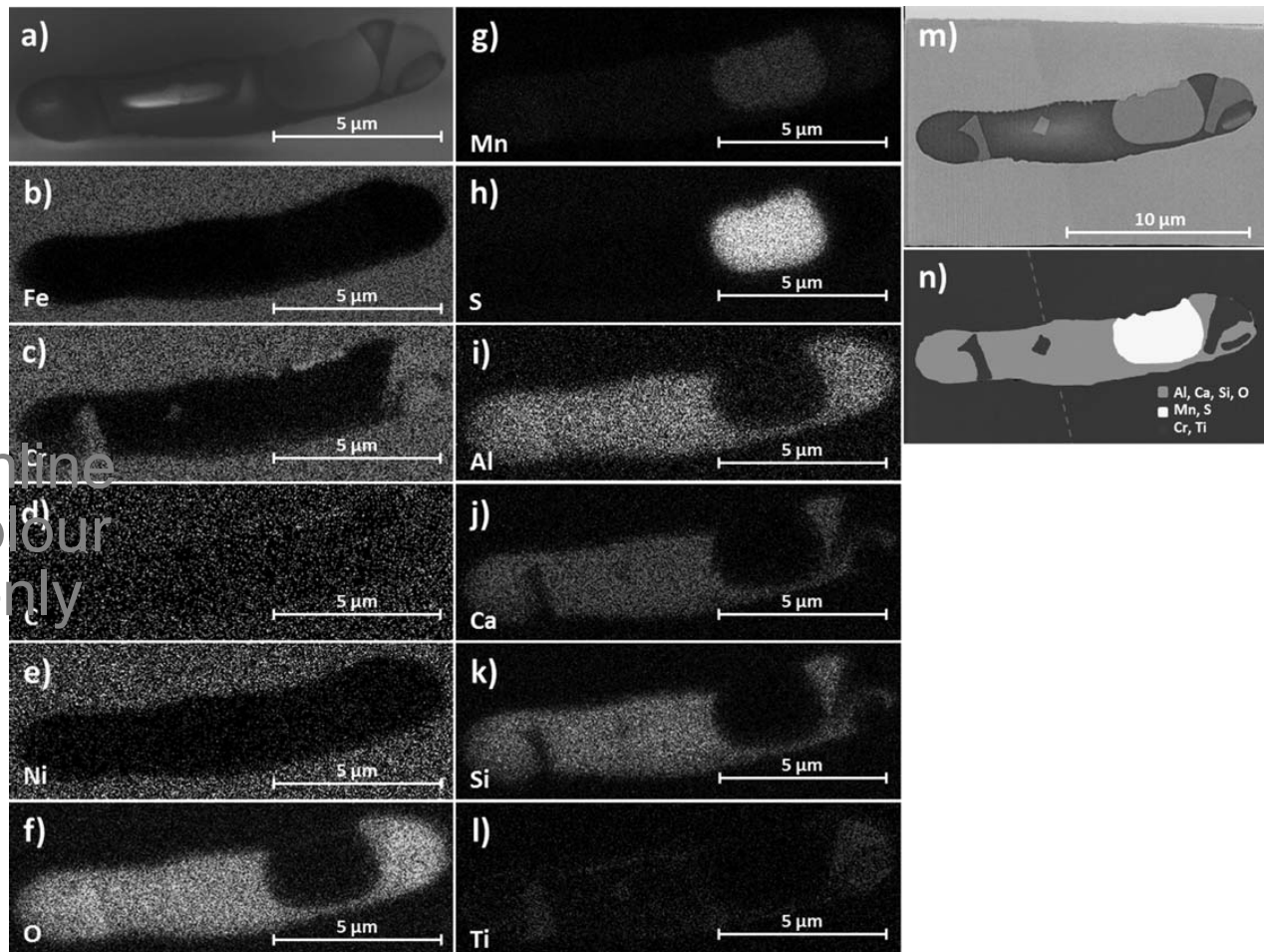
All the cavities have very irregular shapes, e.g. *see* Fig. 7. This can be missed in 2D slices but is quickly revealed in the 3D analysis. As well as the irregular shape of the cavities seen in Figs. 2, 4 and 5, close inspection reveals that almost all of the interfaces are strongly faceted, as seen in Fig. 5k (marked as V) and Fig. 7. The cavities have boundaries with all of the other grain boundary phases identified, and all of them appear more or less faceted. Faceted creep cavities have previously been observed in pure iron,³² a Ni base superalloy,³³ copper³⁴ and α/β brass³⁵ but have not previously been reported in 316 steel. The cavities appear from the FIB-SEM and TEM images to be fairly uniformly spaced along the grain boundary, and for the ~40 cavities measured, we found a maximum single dimension of 2500 nm. Further work segmenting and quantifying the 3D data is required to properly describe the size distribution, although many cavities >1 μm can be clearly seen in Fig. 4.

This faceted cavity shape contrasts with the general assumption made when modelling the development of creep cavities at grain boundaries that isotropic surface tension interacting with a planar boundary will lead to their being lenticular. This assumption requires not only that void growth is diffusion controlled but that 'diffusion is sufficiently fast on the surface of the cavities to maintain their equilibrium lens shape'.³⁶

Stringers

The most abundant features identified by X-ray CT are what have been termed 'stringers'. As can be seen in Fig. 2a, the stringers are aligned roughly along the length of the matchstick, which is parallel to the forming direction in the original component (*see* Figs. 1 and 2a). As seen in Fig. 2c and d for RoI₁, these are cigar shaped particles that have an internal structure not apparent from the X-ray CT data. As described before, they have been detected with a range of sizes, from ~20 μm down to the resolution limit of the X-ray CT imaging (~1 μm). The detailed results of EDX microanalysis of the stringer are shown in Fig. 6. The chemistry of the stringers is complex, and three phases were identified: first, as expected, manganese sulphide; second, a Ca, Al, Si and O rich phase, which must be a silicate inclusion originating from the original casting; and, last, a Cr and Ti rich oxide phase, containing a small amount of Mn. The insulating nature of the silicate phase is apparent from its charging under the electron beam (*see* Fig. 2d, RoI₁). None of the phases contained more than a trace of Fe. The composition and morphology probably originate from the initial casting and forging of the component. This particular stringer sits exactly upon a grain boundary, but one at which there appears to be no secondary phases or cavities. (Later in the preparation of the cross-section, a few cavities were detected at the interface between the stringer and the matrix.) All the stringers examined were in contact with a grain boundary and contained manganese sulphide and the silicate phase.

Generally, the presence of what are usually described just as 'manganese sulphide' inclusions is not seen as a cause for concern,³⁷ although their size suggests that they might act as stress raisers in highly stressed locations, acting as points of initiation for more extensive. The fact that these stringers are not always



6 a image (SEM) (using a mixed signal of secondary and backscatter electrons via 'through lens detector') of stringer imaged from extracted TEM lamella, b-l elemental maps of area shown in a recorded in SEM using EDX spectrum imaging, m backscatter electron image recorded in SEM showing more clearly internal phases as effect of charging is reduced and n schematic diagram showing key to phases identified by EDX spectroscopy

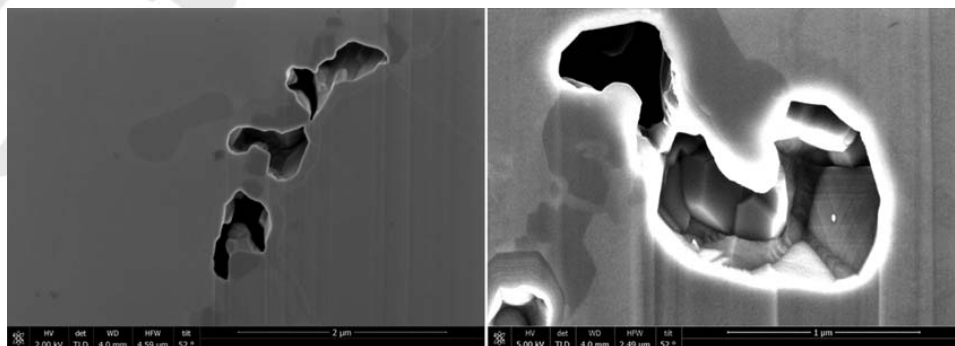
5

associated with cavitated boundaries suggests that, as previously thought, their presence is not critical to the creep behaviour. However, once a crack has started, it is possible that their large size may assist crack propagation, as they may provide an easy path to other nearby cavitated boundaries.

Discussion

Techniques like X-ray CT and SANS are invaluable in providing a statistically significant overview of particles and cavities over large volumes. X-ray CT has the

advantage of accurate spatial mapping in 3D, although, as a rule of thumb, the resolution (which is somewhat bigger than the pixel size) scales with the analysed volume with a multiplication factor of $\sim 1/1000$.¹⁴ In other words 1 μm resolution is possible on a 1 mm diameter specimen and 10 μm resolution attainable on a 10 mm sample. However, in practice, the ability to distinguish different phases is also determined by the contrast between the phases. The high absorption of the X-rays by our steel sample results in noise that reduces the effective spatial resolution. The fact that we can see the 'dark lines' confirms that we have a resolution of the



7 Two SEM images recorded with through lens detector providing mix of backscatter and secondary electrons showing faceted nature of cavities

order of 1–2 μm . The absence of a sharp change in contrast between phases associated with the dark line, the fact that there are multiple different phases and the noise on top of everything result in an uncertainty in identifying the defects in this sample equivalent to about three to four voxels. SANS can, depending on the instrumental set-up, provide volumetric measurement of submicrometre features as reviewed by Rustichelli,³⁸ and is especially powerful in detecting the size and distribution of nanometre sized defects.^{12,30} However, neither of these techniques can necessarily distinguish between secondary phases and cavities, so these measurements must be supported by microscopic analysis of the microstructure.¹¹ Nor are traditional metallographic preparation techniques ideally suited to distinguishing between cavities and secondary phases because the second phases can be inadvertently removed during polishing or etching and the edges of cavities may be rounded. Cross-sections created by FIB sectioning have previously been shown²⁰ to provide a superior preparation method to unambiguously identify cavities separately from secondary phases. In addition, the composition can be determined with submicrometre spatial resolution only by microanalysis of thin foils, and the combination of STEM EDX and SAED provides simultaneous phase identification. This demonstrates that a complete understanding of these complex microstructures requires study of the same area using a combination of techniques.

Microstructure

The intimate association of the cavities with the second phases in the boundary (clearly seen in Figs. 2, 4 and 5) shows that we need to understand the evolution of all the phases in this sample to understand how the local environment around the grain boundaries led to the nucleation of the cavities and affected their growth. At the service temperature of 525°C, volume diffusion of substitutional solutes in 316 steel will be very slow so the nucleation and growth of second phases involving them will be governed by solute supply through grain boundaries and interfaces and along dislocations.

A plastically strained zone would have been created during fabrication by the thermomechanical cycles associated with the original multipass weld. The dislocations in this strain affected zone, extending several millimetres from the weld fusion line, would have provided nucleation sites and rapid diffusion paths for solute supply to create the array of intragranular carbides seen in Fig. 4c and d. Orderly lines of precipitates have been observed (see Fig. 4a and c) close to the grain boundary in this sample similar to those previously found to be nucleated on dislocations.^{39,40} Other intragranular carbides, which do not appear to be aligned, would still be expected to have formed on dislocations. Because the rate of solute supply from the bulk is so limited, the carbides connected by higher diffusivity paths coarsen during aging, leaving a reduced density of intragranular carbides and the carbides along the grain boundary coarsen to micrometre sized particles.²⁹

Ferrite has previously been identified in type 316H stainless steel exposed to creep conditions in different forms, and its presence has been attributed to a range of different sources.⁴¹ The starting material may contain δ ferrite at levels of 1–2%, although a magnaprobe investigation of an unaged header (cast 53579) gave a ferrite content of <0.1%. In addition, welds in this

material are designed to contain an amount of δ ferrite to alleviate hot cracking,^{42,43} so regions close to the fusion boundary may have contained a few wt-% of δ ferrite after welding.

Relatively short exposure (<1000 h) to temperatures of 600°C and above has been shown to be sufficient to completely transform the δ ferrite,⁴⁴ usually forming σ phase and austenite, and sometimes also Laves and χ phase. Tests at 550°C for up to 6200 h^{45,46} have shown stress to accelerate the transformation of δ ferrite in 316 steel, but extrapolating these results suggests that after 65 000 h, <50% of the δ ferrite would have transformed. In another study,⁴⁷ 50% of the delta ferrite had converted to austenite, sigma (σ), chi (χ) and $M_{23}C_6$ after only 5000 h at 500°C. For the sample studied here, which has been exposed to 525°C for 65 000 h, it is therefore possible that some δ ferrite might still be present. If this were the case, it would be expected to have become enriched in Cr and Mo as it transformed to austenite.²⁸ It is this availability of Cr and Mo that would promote the precipitation of σ , χ and Laves phase. However, all the ferrite analysed in the present study was predominantly composed of Fe and was depleted in Cr, Ni and Mo compared to the austenitic matrix, and we have not detected any σ , χ or Laves phase, so this seems to rule out the possibility that the ferrite seen around the grain boundary carbides remains from δ ferrite formed during the manufacture of the header.

Thus, we look to other possible routes for the formation of this ferrite phase. Stewart and Spellward⁴⁸ observed similar triangular ferrite particles up to 1 μm long and of measured composition 91Fe–4Cr–4Ni (wt-%) close to grain boundaries in a similar 316 steel with a similar service history and suggested that this might be the result of ‘supersensitisation’ where, once all the Cr had been incorporated into the carbides, the austenite transforms back to ferrite. No explanation was suggested as to why the removal of Cr (a ferrite former) should result in the FCC to BCC transformation.

The shape of the ferrite seen in the present study and in Ref. 48 is reminiscent of the saw tooth morphology of Widmanstätten ferrite. This is more usually associated with high temperature fcc to bcc transformations in ferritic steels, but Singhal and Martin⁴⁹ found that Widmanstätten ferrite nucleated on $M_{23}C_6$ precipitates in a 24Ni–25Cr austenitic steel aged for 25 h at 750°C. All the ferrite observed in the present study was in contact with $M_{23}C_6$ at a grain boundary and was depleted in Cr, Mo and Ni, but apparently, only Ni was rejected into the surrounding matrix during growth. This suggests that at the comparatively low temperature of 525°C, the diffusion of C was slow enough that, in forming $M_{23}C_6$, the strong carbide formers Cr and Mo might have reduced the local activity of C enough to stabilise ferrite, which, in forming, rejected the austenite forming Ni into the surrounding matrix. Thus, it is unlikely that the ferrite observed around the grain boundaries in this sample originates from the δ ferrite present immediately after the manufacture of the header; the morphology, the composition and the chemistry of its surroundings all point to its having developed during service.

The detrimental influence of extended aging of 316 steel at high temperatures on its creep resistance has, in part, been attributed⁵⁰ to the formation of brittle intermetallic σ phase, which has often been found to replace $M_{23}C_6$

during extended service and appears to be favoured in steels stabilised by Ti or Nb additions.^{51,52} In particular, Morris *et al.* suggest that it is not just that σ phase is brittle but that small $M_{23}C_6$ carbides are replaced by larger σ phase particles, allowing easier grain boundary sliding and higher local stress concentrations. No σ phase was found in the present study. This is in common with a TEM study of 316 steel with a similar composition and service history to that of the present study,^{26,48} which also failed to detect σ phase by X-ray methods after 94 000 h at 600°C, so it appears that at temperatures as low as 525°C, other phases such as σ and χ may not form even after tens of 1000 s of hours.²⁸

Development of cavitation

Here, we consider the nucleation and growth of the cavities and how this occurred in association with the continuing evolution of the phases around the grain boundary.

The residual stress associated with the weld is the main driving force for cavity nucleation in the material surrounding it,⁴ and it is very noticeable that the heavily cavitated boundaries in our sample, seen as 'dark lines' in virtual slices of the X-ray CT data, all lie at close to 45° to the plane of the crack (as described above). This suggests that the shear components of the residual stress field dominated the cavitation behaviour in the HAZ. Voids formed during creep of hydrogen reformer tubes have been observed to form mostly at grain boundaries that were neither perpendicular nor parallel to the hoop stress with those close to the outer wall, in particular, being most likely to lie at 45° to the hoop stress.⁵³ $M_{23}C_6$ is known to form at grain boundaries of similar steels early in the service life of the header, so it is most likely that the $M_{23}C_6$ carbides were present from an early stage and contributed to the formation of the cavities⁴⁷ (as well as to the ferrite as described above). The grain boundaries at 45° to the crack would experience the highest driving force for grain boundary sliding, which would be impeded by the growing $M_{23}C_6$; these and other second phase particles at the boundary would then act as stress raisers. Vacancies would be attracted to relieve the stress built up by the resulting dislocation pile-ups in the boundary around the particles, reducing the nucleation barrier to cavity formation at the carbide/boundary interface. Incoherent interfaces between $M_{23}C_6$ and austenite have been suggested as preferred sites for creep voids.^{54,55} The orientation of the cavitated boundaries is crucial when considering the mechanisms driving the cavity formation. We have observed in our sample a consistent set of findings with respect to the orientation of several cavitated boundaries (*see* the segmented subvolume of the X-ray CT data in Fig. 2a) examined in the region of the weld, but we fully acknowledge the need to extend the volumes analysed as in light of local microstructural inhomogeneities and the complex stress state in this component (*see* Fig. 8 in Ref. 12) to develop greater confidence in the generality of these observations. Superimposed on the effects of the orientation of the grain boundaries planes relative to the principle stresses will be the effects of the crystallographic orientations of the adjoining grains themselves, relative to the principle stresses, relative to the local grain boundary plane and relative to each other. Dzieciol *et al.*³⁴ found a large scatter in the growth rates of individual creep voids in copper and suggested that local dislocation glide made a significant contribution to void growth. They pointed out

that since dislocation glide occurs on particular crystallographic planes, void growth might be expected to depend on the crystallographic orientation of the adjoining grains.

The facetting of creep cavities has been previously been attributed either to the anisotropy of their surface energy or to kinetic effects by which slip on favoured planes will produce faceted voids. Two-dimensional dislocation simulations for example⁵⁶ showed that in single crystals slip could produce facets on originally round voids.

It is not clear whether the ferrite or the cavities nucleated first, but the irregular shape of the cavities and their faceted morphology suggest two alternative mechanisms for their formation. The irregular cavities could have formed either by coalescence of smaller cavities after separate nucleation events or, perhaps, by growth of one initial cavity along the interfaces between the $M_{23}C_6$ carbides and either the matrix or the ferrite as well as along the grain boundary. In either case, continued stress assisted vacancy absorption might be expected to modify normal diffusional growth. The close association between the grain boundary phases and the cavities and the complexity of their interfaces is clearly visible in Figs. 2, 4 and 5 and, while there is still a lot of work to do to understand their evolution, it is clear that the role of the grain boundary phases cannot be ignored.^{57,58} However they are formed, it is clear that for a fixed total volume of cavities (i.e. number of vacancies) the convoluted cavities would cause decohesion over a far wider area of grain surface than the formation of spherical cavities would, leading to a correspondingly higher embrittling effect. Moreover, in the later stages of creep, complex shaped cavities may grow faster than spherical, rod-like or ellipsoidal cavities as observed for a leaded α/β brass by Isaac *et al.*³⁵

If the presence of the grain boundary carbides is critical to the formation of the cavities, it is possible that failure occurred where it did because the dislocations in the HAZ (formed by plastic deformation resulting from the thermal stresses during and after welding) provided additional rapid pathways for solute and/or vacancy supply to the grain boundary region and the intergranular phases, accelerating the formation of cavities in this region. It is also likely that the presence of the ferrite, seen in Fig. 4d, reduced the ductility in the region of the cavitated boundaries, assisting in final fracture.

It is only by exploring and understanding the arrangement of the secondary phases along the grain boundary and their 3D relationship to the dislocation structure that we can hope to then create an accurate model describing the nucleation and growth of the cavities. Additional regions around the crack will be the subject of further investigation.

Conclusions

Multiscale 3D analysis using the correlative tomography approach has allowed us to find key RoIs for high resolution SEM and TEM analysis. In particular X-ray CT analysis has been successfully applied to create a map of the defects buried inside a service aged stainless steel sample and to identify creep damaged zones. Preparation of cross-sections and lamellae using the FIB allowed site specific phase identification and chemical analysis in the regions identified as having the highest propensity for

15

creep cavitation. Scanning electron microscopy, TEM and STEM revealed that the following.

1. The most heavily cavitated boundaries observed in this sample lie parallel to the crack in 2D and at an angle $\sim 45^\circ$ to the plane of the crack in 3D.

2. The surfaces of all cavities appeared faceted.

3. The cavities at the grain boundary were of irregular shape and always connected to secondary phases including $M_{23}C_6$ carbides, ferrite and G phase.

4. The ferrite appeared to have formed during service operation by transformation of the solute depleted austenite in contact with the growing $M_{23}C_6$.

5. Three morphologies of $M_{23}C_6$ carbides were found: large irregular particles up to $\sim 2 \mu\text{m}$ long sitting on the grain boundary and growing into the grains either side forming a discontinuous plate, intermediate particles (100–300 nm) sitting on the grain boundaries but only growing into one grain, and a large population of smaller (45–90 nm) cuboidal intragranular carbides.

6. Because of the intimacy of the contact between the cavities and grain boundary phases, these secondary phases are likely to control where, when and how the cavities themselves form. Cavity growth rates will depend on the local stress and diffusion conditions, which may be very different from those modelled assuming a homogeneous matrix on either side of the grain boundary.

7. ‘Stringers’ were found and identified as predominantly composed of Si, Ca, Al and O associated with manganese sulphide and are silicate inclusions from the original cast.

The complexity and faceted morphology of cavitated grain boundaries decorated with carbides of varying size, ferrite and G phase suggest that current models that are used to predict the lifetime of components, based on the nucleation and growth of spherical cavities, are oversimplified.

Further work will focus on a 3D nanoscale analysis of the decorated grain boundaries and on mapping the cavity sizes and morphologies and the microstructural variations in further volumes and chosen from both regions of low to high creep damage, with the aim of understanding the evolution of creep damage from initiation to rupture.

Acknowledgements

We acknowledge FEI funding of TLB. Useful comments and help from T. Slater and M. G. Burke, BP ICAM funding of PJW and SAM, EDF Energy for the supply of the test component and funding for HJ. R. Mokso at the TOMCAT beamline at the Swiss Light Source. We are grateful to the EPSRC whose grant funding (grant nos. EP/I02249X, EP/F007906 and EP/F028431) enabled the purchase and support of the imaging equipment in the Henry Moseley X-ray Imaging Facility. The FEI Titan G2 is funded by HM Government (UK) and is associated with research capability of the Nuclear Advanced Manufacturing Research Centre.

References

1. R. W. Evans and B. Wilshire: ‘Creep of metals and alloys’; 1985, London, Institute of Metals.
2. ‘R5 assessment procedure for the high temperature response of structures’, Issue 3, Revision 001, EDF Energy Nuclear Generation Ltd, 2012.

3. C. Gupta, H. Toda, P. Mayr and C. Sommitsch: ‘The 3D nature of creep cavitation and its implications for residual life estimation methods in heat resistant steels: a critical review’, *Mater. Sci. Technol.*, to be published.
4. M. Turski, P. J. Bouchard, A. Steurer and P. J. Withers: ‘Residual stress driven creep cracking in type 316 stainless steel’, *Acta Mater.*, 2008, **56**, 3598–3612.
5. C. D. Lundin, P. Liu and Y. Cui: ‘A literature review on characteristics of high temperature ferritic Cr–Mo steels and weldments’; 2000, New York, Welding Research Council.
6. M. P. O’Donnell, R. A. W. Bradford, D. W. Dean, C. D. Hamm and M. Chevalier: ‘Structural integrity of nuclear power plant: high temperature issues in advanced gas cooled reactors (AGR)’, 1; 2013, Abington, EMAS Publishing.
7. M. C. Coleman, D. A. Miller and R. A. Stevens: ‘Reheat cracking and strategies to assure integrity of type 316 weld components’, Proc. Int. Conf. on ‘Integrity of high temperature welds’, PEP Ltd, London, UK, 1998, 169–179.
8. R. Hales: ‘Method of creep damage summation based on accumulated strain for the assessment of creep-fatigue endurance’, *Fatigue Fract. Eng. Mater. Struct.*, 1983, **6**, 121–135.
9. M. W. Spindler: *Fatigue Fract. Eng. Mater. Struct.*, 2004, **27**, 273–281.
10. J. Yu, X. Lin, J. Wang, J. Chen and W. Huang: ‘First-principles study of the relaxation and energy of bcc-Fe, fcc-Fe and AISI-304 stainless steel surfaces’, *Appl. Surf. Sci.*, 2009, **255**, 9032–9039.
11. H. Jazaeri, P. J. Bouchard, M. T. Hutchings and P. Lindner: ‘Study of creep cavitation in stainless steel weldment’, *Mater. Sci. Technol.*, 2014, **30**, 38–42.
12. P. J. Bouchard, P. J. Withers, S. A. McDonald and R. K. Heenan: ‘Quantification of creep cavitation damage around a crack in a stainless steel pressure vessel’, *Acta Mater.*, 2004, **52**, 23–34.
13. H. Jazaeri, P. J. Bouchard, M. Hutchings, A. A. Mamun and R. K. Heenan: ‘Application of small angle neutron scattering to study creep cavitation in stainless steel weldments’, *Mater. Sci. Technol.*, to be published.
14. E. Maire and P. J. Withers: ‘Quantitative X-ray tomography’, *Int. Mater. Rev.*, 2014, **59**, 1, 1–43.
15. A. Pyzalla, B. Camin, T. Buslaps, M. Di Michiel, H. Kaminski, A. Kottar, A. Pernack and W. Reimers: ‘Simultaneous tomography and diffraction analysis of creep damage’, *Science*, 2005, **308**, 5718, 92–95.
16. C. Gupta, H. Toda, C. Schlacher, Y. Adachi, P. Mayr, C. Sommitsch, K. Uesugi, Y. Suzuki, A. Takeuchi and M. Kobayashi: ‘Study of creep cavitation behaviour in tempered martensitic steel using synchrotron micro-tomography and serial sectioning techniques’, *Mater. Sci. Eng. A*, 2013, **A564**, 525–538.
17. F. Sket, A. Isaac, K. Dzieciol, G. Sauthoff, A. Borbely and A. R. Pyzalla: ‘In situ tomographic investigation of brass during high-temperature creep’, *Ser. Mater.*, 2008, **59**, 558–561.
18. A. Isaac, F. Sket, W. Reimers, B. Camin, G. Sauthoff and A. R. Pyzalla: ‘In situ 3D quantification of the evolution of creep cavity size, shape, and spatial orientation using synchrotron X-ray tomography’, *Mater. Sci. Eng. A*, 2008, **A478**, 108–118.
19. A. Kyrielleis, V. Titarenko, M. Ibson, T. Connelly and P. J. Withers: ‘Region-of-interest tomography using filtered back-projection: assessing the practical limits’, *J. Microsc.*, 2011, **241**, 69–82.
20. B. Chen, P. E. J. Flewitt, D. J. Smith and C. P. Jones: ‘An improved method to identify grain boundary creep cavitation in 316H austenitic stainless steel’, *Ultramicroscopy*, 2011, **111**, 309–313.
21. T. L. Burnett et al.: ‘Correlative tomography’, *Sci. Rep.*, 2014, **4**, 4711.
22. H. Jazaeri, B. K. Chong, P. J. Bouchard, A. Rao and J. A. J. James: ‘Characterization of creep damage in a type 316H stainless steel weldment using synchrotron X-ray tomography and microscopic examination’, *Metall. Mater. Trans. A*, to be published.
23. M. A. Groeber, B. K. Haley, M. D. Uchic, D. M. Dimiduk and S. Ghosh: ‘3D reconstruction and characterization of polycrystalline microstructures using a FIB-SEM system’, *Mater. Charact.*, 2006, **57**, 259–273.
24. J. K. L. Lai: ‘A review of precipitation behaviour in AISI type 316 stainless steel’, *Mater. Sci. Eng.*, 1983, **61**, 101–109.
25. B. Weiss and R. Stickler: ‘Phase instabilities during high temperature exposure of 316 austenitic stainless steel’, *Metall. Mater. Trans. B*, 1972, **3B**, (4), 851–866.
26. J. K. L. Lai: ‘A study of precipitation in AISI type 316 stainless steel’, *Mater. Sci. Eng.*, 1983, **58**, (2), 195–209

27. T. Sourmail: 'Precipitation in creep resistant austenitic stainless steels', *Mater. Sci. Technol.*, 2001, **17**, 1–14.
28. J. J. Smith and R. A. Farrar: 'Influence of microstructure and composition on mechanical properties of some AISI 300 series weld metals', *Int. Mater. Rev.*, 1993, **38**, 25–51.
29. Y. Minami, H. Kimura and Y. Ihara: 'Microstructural changes in austenitic stainless steels during long-term aging', *Mater. Sci. Technol.*, 1986, **2**, 795–806.
30. M. T. Hutchings: 'The use of small angle neutron scattering for mapping creep cavitation damage in an ex-service steam header', OU/MatsEng/025, The Open University, 2012, 1–26.
31. D. J. Powell et al.: 'The precipitation characteristics of 20% Cr/25% Ni–Nb stabilised stainless steel', *Acta Metall.*, 1988, **36**, (3), 713–724.
32. D. M. R. Taplin and A. L. Wingrove: 'Study of intergranular cavitation in iron by electron microscopy of fracture surfaces', *Acta Metall.*, 1967, **15**, (7), 1231–1236.
33. T. Link et al.: 'Synchrotron tomography of porosity in single-crystal nickel-base superalloys', *Mater. Sci. Eng. A*, 2006, **A425**, (1–2), 47–54.
34. K. Dzieciol et al.: 'Void growth in copper during high-temperature power-law creep', *Acta Mater.*, 2011, **59**, (2), 671–677.
35. A. Isaac et al.: 'In situ 3D quantification of the evolution of creep cavity size, shape, and spatial orientation using synchrotron X-ray tomography', *Mater. Sci. Eng. A*, 2008, **A478**, (1–2), 108–118.
36. M. Vöse, B. Fedelich and J. Owen: 'A simplified model for creep induced grain boundary cavitation validated by multiple cavity growth simulations', *Comput. Mater. Sci.*, 2012 **58**, 201–213.
37. M. Spindler, private communication.
38. F. Rustichelli: 'Applications of small neutron scattering in material science and technology', *Metall. Sci. Technol.*, 1993, **11**, 118–141.
39. F. R. Beckitt and B. R. Clark: 'The shape and mechanism of formation of $M_{23}C_6$ carbide in austenite', *Acta Metall.*, 1967, **15**, (1), 113–129.
40. M. H. Lewis and B. Hattersley: 'Precipitation of $M_{23}C_6$ in austenitic steels', *Acta Metall.*, 1965, **13**, (11), 1159–1168.
41. A. D. Warren, P. E. J. Flewitt and T. B. Scott, private communication.
42. F. C. Hull: 'Effect of delta ferrite on the hot cracking of stainless steel', *Weld. J.*, 1967, **46**, (9), 399–s–409–s.
43. J. C. Lippold and W. F. Savage: 'Solidification of austenitic stainless steel weldments. Part III: the effect of solidification behavior on hot cracking susceptibility', *Weld. Res. Suppl.*, 1982, **1**, 388–396s.
44. G. Sasikala, S. K. Ray and S. L. Mannan: 'Kinetics of transformation of delta ferrite during creep in a type 316(N) stainless steel weld metal', *Mater. Eng. A*, 2003, **A359**, 86–90.
45. M. D. Mathew, G. Sasikala, S. L. Mannan and P. Rodriguez: 'Transformation of ferrite in type 316 stainless steel weld metal during creep deformation', *Mater. Sci. Technol.*, 1991, **7**, 533–535.
46. M. D. Mathew, G. Sasikala, S. L. Mannan and P. Rodriguez: 'Effect of stress on the transformation behaviour of delta-ferrite in type 316 stainless steel weld metal', *J. Mater. Sci. Lett.*, 1994, **13**, 194–196.
47. T. P. S. Gill, M. Vijayalakshmi, J. B. Gnanamoorthy and K. A. Padmanabhan: 'Transformation of delta-ferrite during the post-weld heat treatment of type 316L stainless steel weld metal', *Weld. Res. Suppl.*, 1986, 123–s.
48. D. A. Stewart and P. Spellward: 'Transmission electron microscopy investigation of materials originating from Heysham 1 Header 2D22', M/TE/EXT/REP/0163/00.
49. L. K. Singhal and J. W. Martin: 'The formation of ferrite and sigma-phase in some austenitic stainless steels', *Acta Metall.*, 1968, **16**, 1441–1451.
50. D. Morris: 'The influence of sigma phase on creep ductility in type 316 stainless steel', *Scr. Metall.*, 1979, **13**, (12), 1195–1196.
51. J. Barcik: 'Mechanism of sigma-phase precipitation in Cr–Ni stainless steels', *Mater. Sci. Technol.*, 1988, **4**, (1), 5–15.
52. C. C. Hsieh and W. Wu: 'Overview of intermetallic sigma (σ) phase precipitation in stainless steels', *ISRN Metall.*, 2012.
53. A. A. Wahab et al.: 'A three-dimensional characterization of creep void formation in hydrogen reformer tubes', *Scr. Mater.*, 2006, **55**, (1), 69–73.
54. A. A. Wahab and M. V. Kral: '3D analysis of creep voids in hydrogen reformer tubes', *Mater. Sci. Eng. A*, 2005, **A412**, (1–2), 222–229.
55. H. U. Hong and S. W. Nam: 'Improvement of creep-fatigue life by the modification of carbide characteristics through grain boundary serration in an AISI 304 stainless steel', *J. Mater. Sci.*, 2003, **38**, (7), 1535–1542.
56. J. Segurado and J. Llorca: 'Discrete dislocation dynamics analysis of the effect of lattice orientation on void growth in single crystals', *Int. J. Plast.*, 2010, **26**, (6), 806–819.
57. G. B. Sarma and B. Radhakrishnan: 'Modeling the effect of microstructural features on the nucleation of creep cavities', *Mater. Sci. Eng. A*, 2008, **A494**, 92–102.
58. D. Li and K. Shinozaki: 'Simulation of role of precipitate in creep void occurrence in heat affected zone of high Cr ferritic heat resistant steels', *Sci. Technol. Weld. Join.*, 2005, **10**, (5), 544.

Authors Queries













Journal: **Materials Science and Technology**





Paper: **11542**

Title: **Multiscale 3D analysis of creep cavities in AISI type 316 stainless steel**

Dear Author

During the preparation of your manuscript for publication, the questions listed below have arisen. Please attend to these matters and return this form with your proof. Many thanks for your assistance

Query Reference	Query	Remarks 
1	Please confirm the running head is correct.	
2	Fig. 2 will be reproduced in mono for the printed version. Please check if extra explanation or a new figure is needed.	
3	Fig. 4 will be reproduced in mono for the printed version. Please check if extra explanation or a new figure is needed.	
4	Fig. 5 will be reproduced in mono for the printed version. Please check if extra explanation or a new figure is needed.	
5	Fig. 6 will be reproduced in mono for the printed version. Please check if extra explanation or a new figure is needed.	
6	Please update information for Ref. 3.	
7	Please update information for Ref. 13.	
8	Please update information for Ref. 22 and the names of the other authors.	
9	Please supply the names of the other authors for Ref. 31.	
10	Please supply the names of the other authors for Ref. 33.	
11	Please supply the names of the other authors for Ref. 34.	

12	Please supply the names of the other authors for Ref. 35.	
13	Please supply the volume number and page range for Ref. 52.	
14	Please complete the sentence "This paper is part of a special issue on...".	
15	There's no Fig.8, plesae check.	

Maney Publishing
Not For Distribution